Micromechanical modeling and experimental characterization for the elastoplastic behavior of a functionally graded material

Liangliang Zhang [a,b,1,*], Qiliang Lin [b,1], Fangliang Chen [c], Yanchu Zhang [b], Huiming Yin [b]

[a] Department of Applied Mechanics, China Agricultural University, Room 301 Yifu Building, 17 Qinghua East Road, Beijing, Beijing 100083, China
[b] Department of Civil Engineering and Engineering Mechanics, Columbia University, 610 Seeley W. Mudd 500 West 120th Street, New York, NY 10027, USA
[c] Virtual Construction Lab of Schüco, New York 10018, USA

ABSTRACT

Functionally Graded Materials (FGMs) are characterized by the distribution in composition and structure gradually over volume, which were recently designed and developed as a key component of a multifunctional building envelope for the high performance of energy efficiency. It was realized by mixing aluminum particles and fine High-Density Polyethylene (HDPE) powders through a vibration-sedimentation process. To investigate the elastoplastic behavior of FGMs, an elastoplastic model based on micromechanics with pairwise particle interactions is developed in this study. The particle phase is assumed to remain in its linearly elastic state while the matrix phase undergoes elastoplastic deformation. The corresponding yield function for the FGMs is investigated, where the pairwise interaction and probabilistic spatial distribution of particles are utilized to accommodate the gradation of particle volume fraction. Accordingly, the overall elastoplastic behavior of FGMs is established through the microscopic homogenization. The proposed algorithm is validated with uniaxial compression test of FGM samples, where the authentic particle distribution is captured statistically through image processing method. Finally, the effect of volume fraction distributions on the overall effective elastoplastic behavior of FMGs is investigated.

© 2020 Elsevier Ltd. All rights reserved.

1. Introduction

Functionally graded materials (FGMs) are often characterized by the continuous distribution (Kumar and Dutta, 1998) in composition and structure over volume fraction. Within FGMs, different microstructural phases have different properties, and the overall FGMs attain the multifunctional status from their property gradation, enabling various multifunctional tasks by virtue of spatially tailored microstructures (Yin et al., 2004). FGMs are initially designed for thermal barrier in aerospace application (Koizumi, 1997), however, thanks to its various devisable properties, it has exhibited enormous applications in many industrial field, such as bioengineering (Pompe et al., 2003), nuclear (Gasik, 1998), electric engineering (Kurimoto et al., 2010), civil engineering (Chen et al., 2016), and so on. For example, a novel two-phase FGM was developed in a building integrated photovoltaic thermal (BIPVT) roofing

panel, which helps leading the conversion efficiency of solar energy to achieve a considerable level by cooling down the temperature of solar cells.

This BIPVT roofing system is schematically illustrated in Fig. 1 (Chen et al., 2016), in which the two-phase FGM layer (Al/HDPE layer) gradually transits material phases from metal dominated to polymer dominated. On the top surface, the high aluminum concentration creates a high thermal conductivity to make sure that the heat can be transferred to water tubes immediately and taken away by water flow; while at the bottom surface, pure HDPE is used to insulate the heat from entering to the building so as to improve the thermal comfort inside the building. The main multifunctional FGM layer enhances the energy conversion efficiency and improves the lifespan of PV cells as well. Due to the variation of the effective thermal expansion coefficient along the gradation direction, the FGM may exhibit curling behavior during the manufacture, which should be well controlled in the applications (Lin et al., 2017). Similarly, significant thermo-elasto-plastic deformation may be induced in the FGM layer under the direct sun light, especially in sun-drenched locations. Therefore, the elastoplastic analysis of the FGM plays an important role to keep the panel's curvature in the design BIPVT roofing system.

---

* Corresponding author.
  E-mail addresses: llzhang@cau.edu.cn (L. Zhang), ql2241@columbia.edu (Q. Lin), fangliang.chen@columbia.edu (F. Chen), yz3473@columbia.edu (Y. Zhang), yin@civil.columbia.edu (H. Yin).
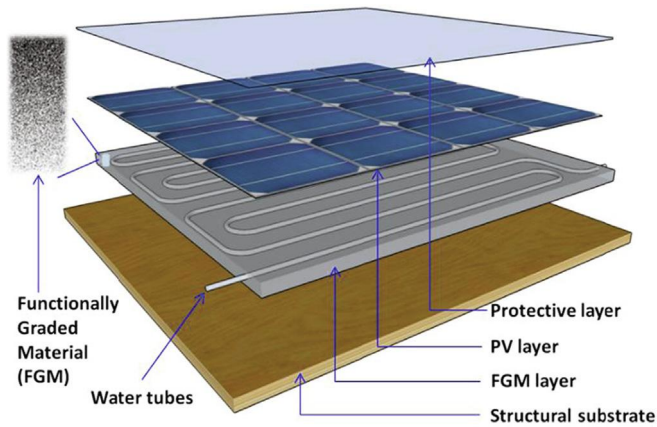 [1] Equal contribution

Fig. 1. A hybrid solar roofing panel integrating an FGM plate with other layers for heat harvesting and temperature control.

In virtue of its heterogeneous nature, the analytical schemes to tackle the spatial variation of each phase within FGMs are limited in the literature. Historically, Eshelby (1957), Eshelby (1959) developed the equivalent inclusion method (EIM) to study the elastic field of a single inhomogeneity within an infinite matrix domain, in which the difference of material properties mismatch between particle and matrix is represented by the eigenstrain. In this paper, following Mura's definition (Mura, 2013), the concept "inhomogeneity" is defined as a sub-domain Ω in domain D, where the elastic moduli in Ω and $D - \Omega$ are assumed to be different, while the concept "inclusion" is defined as the elastic moduli in each domain are assumed to be the same. Moschovidis and Mura (1975) further modified and extended this method to address the multi-particle problem and ellipsoidal shape. Effective medium approaches take into account the effect of the occurrence of the particles on the averaged material properties and the average elastic field of the matrix, and then predict effective elastic properties of composites regardless of the particle distributions and microstructure. Examples include Mori-Tanaka (Mori and Tanaka, 1973), self-consistent (Hill, 1965), the differential scheme (McLaughlin, 1977; Hashin, 1988), and the generalized self-consistent model (Christensen and Lo, 1979). In terms of FGMs, by using of EIM, Zuiker (1995) considered the Mori-Tanaka, self-consistent and Tamura's models among comparisons of standard micromechanical techniques. After that, a comparison between the Mori-Tanaka, self-consistent models and the finite element simulation of FGM was also presented in Refs (Reiter et al., 1997; Reiter and Dvorak, 1998). However, those models did not directly analyze the interaction between particles. When the variation is relatively smooth, standard homogenization methods such as Mori-Tanaka model and self-consistent model can be applied, while higher order generalized theories should be used (Aboudi et al., 2003; Nemat-Nasser and Hori, 2013) when the gradation is sharp. In addition, finite element models (Nguyen-Xuan et al., 2011; Pascon and Coda, 2015; Jrad et al., 2018; Mallek et al., 2019; Bouhamed et al., 2019) based on micromechanics have been widely used to predict the material properties of FGMs. However, these methods were computationally intensive and inconvenient to be implemented for engineering and structural analysis, when the local particle interactions are considered.

The micromechanics based homogenization method has been widely utilized to analyze the elastoplastic (Vena et al., 2008; Barai and Weng, 2011; Aghababaei and Joshi, 2011; Ortwein et al., 2014; Amirpour et al., 2017) and viscoplastic (Li and Weng, 2007; Pierard et al., 2007; Chen and Ghosh, 2012; Brassart et al., 2012; Lahellec and Suquet, 2013; Agoras et al., 2016) problems

of two-phase composites. In recent years, it is considered an effective approach to analyze the FGMs (Birman and Byrd, 2007; Yin and Zhao, 2016), where the materials are homogenized locally in the representative volume element (RVE) at the microscopic scale to achieve globally heterogeneous behavior at the macroscopic scale. Based on EIM, Ju and Chen (1994a), Ju and Chen (1994b) presented the elastic prediction of particle-reinforced metal matrix composites (PRMMC) with spherical and spheroidal particles. After that, Ju and Chen (1994c) also studied the effective elastoplastic deformations and responses of PRMMC by introducing the "effective yield criterion", which is derived micromechanically by considering effects of elastic spherical particles embedded in the elastoplastic matrix. Ju and Tseng (1996), Ju and Tseng (1997) further extended this theory by considering the pairwise spherical particle interaction in particle reinforced ductile matrix composites, and they derived analytical expressions for the bulk and shear moduli of a two-phase composite. Built upon this, Ju and Sun (2001) and Sun and Ju (2001) proposed an expression for the overall elastoplastic stress–strain of randomly located, aligned spheroid reinforced metal matrix composites. Furthermore, elastoplastic responses of metal matrix composites with more complicated particle distribution (i.e., randomly located and randomly oriented particles in the matrix) were developed by Sun and Ju (2004). In recent years, Mareau and Berbenni (2015) developed a novel self-consistent modeling based on the translated field method to study the elasto-viscoplastic problems of fiber-reinforced composites and polycrystalline materials. A granular micromechanics model by using of grain-scale force–displacement relationships was built by Misra and Yang (2010) to study the cohesive materials. This approach was also extended to study the rate-dependent materials (Misra and Singh, 2013) as well as the cementitious materials with thermal effect (Misra and Poorsolhjouy, 2015).

As FGMs with metallic/polymeric matrix are extensively used in the industry field under externally applied mechanical or thermal loadings, plastic deformation is inevitably occurred in the metallic/polymeric matrix. Therefore, the elastoplastic analysis of the FGMs is highly desired to accurately characterize their elastoplastic behavior. Nevertheless, the studies of elastoplastic problems of FGMs are rare in the literature. Gasik (1998) developed a Gasik-Ueda model to study the elastoplastic behavior of FGMs. In his study, the dilute model was used to develop the elastoplastic behavior of plates. However, the model failed to consider the particle interactions and could not be applied to FGMs with high particle volume fraction. After that, Yin et al. (2004) developed an elastic algorithm based on the micromechanics scheme to accommodate the graded nature of FGMs, which considered the particle pairwise interactions and coupling effect of neighboring layers. The method was later extended to interfacial debonding (Paulino et al., 2006) as well as thermomechanical (Yin et al., 2008) behaviors.

In this study, the elastoplastic behavior of metal- and polymer-matrix FGMs is micromechanically modeled by considering the pairwise interaction between particles and the coupling effect between neighboring layers. An image-based analysis method is developed to statistically capture the authentic particle distribution of the FGM. The two-phase FGM is studied, with the assumption that the plastic deformation only occurs in the matrix phase (HDPE phase). This paper will formulate the problem, implement the algorithm, and validate the model with the experiments. The rest of the paper is organized as follows. In Section 2, a brief framework of micromechanics and its application to the elastic analysis of FGMs is provided. In Section 3, the corresponding plastic algorithm is discussed, where the ensemble average yield function is introduced with the corresponding stress norm. In Section 4, experimental validation of the proposed method is provided and discussed. In Section 5, the effect of the particle overall volume fraction and its distribution function to the elastoplastic behavior

of FGMs are numerically studied. Finally, some conclusive remarks are provided in the last section.

2. Micromechanical framework

2.1. Micromechanics-based model with EIM

In this subsection, a brief review of the elastic formulation is given to introduce the background and to formulate a complete elastoplastic algorithm based on our previous work (Yin et al., 2004; Yin and Zhao, 2016; Lin et al., 2019). Both the particle and the matrix phase are assumed to be in the elastic domain. A particle embedded in an infinite matrix under far field strain $\boldsymbol{\varepsilon}^0$ is considered, and the local strain field at a certain point $\boldsymbol{x}$ is decomposed into the far field strain and the disturbed strain $\boldsymbol{\varepsilon}$,

$$\boldsymbol{\varepsilon} = \boldsymbol{\varepsilon}^0 + \boldsymbol{\varepsilon}' \tag{1}$$

where the disturbed strain $\boldsymbol{\varepsilon}'$ represents the elastic mismatch between the particle and the matrix and is computed through the modified Green's function $\boldsymbol{G}(\boldsymbol{x}, \boldsymbol{x})$:

$$\boldsymbol{\varepsilon}' = -\int_{\Omega} \boldsymbol{G}(\boldsymbol{x}, \boldsymbol{x}') \cdot \boldsymbol{C}_0 : \boldsymbol{\varepsilon}^*(\boldsymbol{x}') d\boldsymbol{x}' \tag{2}$$

where Ω represents the particle domain, $\boldsymbol{C}_0$ and $\boldsymbol{C}_1$ are the elastic stiffness tensor of the matrix and the particle, respectively. $\boldsymbol{\varepsilon}^*$ is the eigenstrain which represents the material mismatch under the external load. For a single inhomogeneity problem, as is shown in Fig. 2, the stress equivalent condition around the spherical particle domain Ω is derived as:

$$\boldsymbol{C}_1 : (\boldsymbol{\varepsilon}^0 + \boldsymbol{\varepsilon}') = \boldsymbol{C}_0 : (\boldsymbol{\varepsilon}^0 + \boldsymbol{\varepsilon}' - \boldsymbol{\varepsilon}^*) \tag{3}$$

where the eigenstrain $\boldsymbol{\varepsilon}^*$ is related to the disturbed strain $\boldsymbol{\varepsilon}'$ and is derived as:

$$\boldsymbol{\varepsilon}^* = \boldsymbol{C}_0^{-1} \cdot \left(\boldsymbol{D}^{\Omega} - \Delta\boldsymbol{C}^{-1}\right)^{-1} : \boldsymbol{\varepsilon}^0 \tag{4}$$

In Eq. (4), $\Delta\boldsymbol{C} = \boldsymbol{C}_1 - \boldsymbol{C}_0$ is the stiffness difference and $\boldsymbol{D}^{\Omega}$ signifies the integral of the modified Green's function within the spherical particle domain Ω, and is formulated as:

$$D_{ijkl}^{\Omega} = \frac{1}{30\mu(1-v)} \left[\delta_{ij}\delta_{kl} - (4 - 5v)(\delta_{ik}\delta_{jl} + \delta_{il}\delta_{jk})\right] \tag{5}$$

Combining Eqs. (1), (2) and (4), the strain field within the spherical particle domain is shown to be uniform as:

$$\overline{\boldsymbol{\varepsilon}} = \left(\boldsymbol{I} - \boldsymbol{D}^{\Omega} \cdot \Delta\boldsymbol{C}\right)^{-1} : \boldsymbol{\varepsilon}^0 \tag{6}$$

where $\boldsymbol{I}$ signified the fourth-rank symmetric identity tensor $I_{ijkl} = \frac{1}{2}(\delta_{ik}\delta_{jl} + \delta_{il}\delta_{jk})$.

Moschovidis and Mura (1975) extended the above scheme to two spherical particles embedded in an infinite matrix domain. With the help of the polynomial expansion, the averaged strain field within each particle domain is derived as:

$$\overset{\iota_{\dot{c}}}{\boldsymbol{\varepsilon}} = \frac{1}{V_{\Omega}} \int_{\Omega} \boldsymbol{\varepsilon} d\Omega = \left(\boldsymbol{I} - \boldsymbol{D}^{\Omega} \cdot \Delta\boldsymbol{C} - \boldsymbol{D} \cdot \Delta\boldsymbol{C}\right)^{-1} : \boldsymbol{\varepsilon}^0 + O(\rho^8) \tag{7}$$

where $\rho = a/b$ and $V_{\Omega} = 4\pi a^3/3$ with a and b being the particle radius and the center-to-center distance between the two particles centered at $\boldsymbol{x}_1$ and $\boldsymbol{x}_2$, respectively. $\boldsymbol{D}$ represents the integral of the modified Green's function inside the matrix domain, where the other particle is located. Following the notification of Ju and Chen (1994b), the fourth order tensor D_{ijkl} has the form $D_{ijkl}(D_m)$, and its parameters D_m are elaborated in the appendix Eq. (A2). Eq. (7) represents the volume average strain within each particle

with the influence of the other particle and its precision can reach the order of $O(\rho^8)$, where ρ is not higher than 0.5. Comparing Eqs. (6)–(7), the average influence of one particle to the other is derived as:

$$\boldsymbol{d}(\boldsymbol{x}_1, \boldsymbol{x}_2) = \overset{\iota_{\dot{c}}}{\boldsymbol{\varepsilon}} - \overline{\boldsymbol{\varepsilon}} = \Delta\boldsymbol{C}^{-1} \cdot \boldsymbol{L}(\boldsymbol{x}_1, \boldsymbol{x}_2) : \boldsymbol{\varepsilon}^0 \tag{8}$$

where the particle pairwise interaction tensor $\boldsymbol{L}(\boldsymbol{x}_1, \boldsymbol{x}_2)$ is:

$$\boldsymbol{L}(\boldsymbol{x}_1, \boldsymbol{x}_2) = \left(\left[\Delta\boldsymbol{C}^{-1} - \boldsymbol{D}^{\Omega} - \boldsymbol{D}\right]^{-1} - \left[\Delta\boldsymbol{C}^{-1} - \boldsymbol{D}^{\Omega}\right]^{-1}\right) + O(\rho^8) \tag{9}$$

The explicit expression of $\boldsymbol{L}$ can be found in the appendix Eq. (A3). It is noted that Eq. (8) can be extended to represent the pairwise interactions of multiple particles $P_i(i = 2, 3, \cdots)$ to one particle $P_1(\boldsymbol{x}_1)$, such that for a given particle configuration $\mathcal{G}$ with N particles, the average strain of $P_1(\boldsymbol{x}_1)$ domain with pairwise particle interactions is given as:

$$\overset{\iota_{\dot{c}}}{\boldsymbol{\varepsilon}}(\boldsymbol{x}_1) = \left(\boldsymbol{I} - \boldsymbol{D}^{\Omega} \cdot \Delta\boldsymbol{C}\right)^{-1} : \boldsymbol{\varepsilon}^0 + \sum_{i=2}^{N} \boldsymbol{d}(\boldsymbol{x}_1, \boldsymbol{x}_i) \tag{10}$$

2.2. Effective elastic behavior of FGMs based on micromechanics

In this subsection, a brief review of elastic formulation of FGMs is given based on our previous work (Yin et al., 2004; Yin and Zhao, 2016; Lin et al., 2019). As shown in Fig. 3, the gradation direction of typical FGMs is assumed along the $X_3(x_3)$ direction with a microscopic RVE and a microscopic coordinate $\boldsymbol{x}$, at the macroscopic point $\boldsymbol{X}$. Within the RVE, the particle distribution is graded in x_3 direction. Without loss of generality, it is assumed that one particle P_1 exists at the center $\boldsymbol{x} = 0$ of the RVE. With the help of Eq. (10), the averaged strain inside the P_1 domain is given as:

$$\langle\boldsymbol{\varepsilon}\rangle^{P_1} = \left(\boldsymbol{I} - \boldsymbol{D}^{\Omega} \cdot \Delta\boldsymbol{C}\right)^{-1} : \boldsymbol{\varepsilon}^0(P_1) + \sum_{i=2}^{\infty} \Delta\boldsymbol{C}^{-1} \cdot \boldsymbol{L}(P_1, P_i) : \boldsymbol{\varepsilon}^0(P_i) \tag{11}$$

where $\boldsymbol{\varepsilon}^0(P_i)$ represents the prescribed far field strain at the same height of the corresponding particle P_i, and varies along the microscopic field with particle volume fraction, such that the above equation can be further written as:

$$\langle\boldsymbol{\varepsilon}\rangle(0) = \left(\boldsymbol{I} - \boldsymbol{D}^{\Omega} \cdot \Delta\boldsymbol{C}\right)^{-1} : \boldsymbol{\varepsilon}^0(0) + \sum_{i=1}^{\infty} \Delta\boldsymbol{C}^{-1} \cdot \boldsymbol{L}(0, \boldsymbol{x}^i) : \boldsymbol{\varepsilon}^0(x_3^i) \tag{12}$$

The prescribed far field strain $\boldsymbol{\varepsilon}^0(x_3^i)$ is related to the far field strain at the center of the RVE $\boldsymbol{\varepsilon}^0(0)$ by the Taylor expansion to the first order:

$$\boldsymbol{\varepsilon}^0(x_3^i) \cong \boldsymbol{\varepsilon}^0(0) + \boldsymbol{\varepsilon}_{,3}^0(0)(\boldsymbol{x}^i - 0) = \boldsymbol{\varepsilon}^0(0) + \boldsymbol{\varepsilon}_{,3}^0(0)x_3 \tag{13}$$

Since all particles are statistically distributed microscopically in a random way, a probability function $P(\boldsymbol{x}|0)$ is introduced to statistically represent the probability to have a particle centered at×, given another particle at $\boldsymbol{0}$. Therefore, the summation of the pairwise interaction is converted into integral over all possible particle positions as follows:

$$\langle\boldsymbol{d}\rangle(0) = \sum_{i=1}^{\infty} \Delta\boldsymbol{C}^{-1} \cdot \boldsymbol{L}(0, \boldsymbol{x}^i) : \boldsymbol{\varepsilon}^0(x_3^i) = \int_D P(\boldsymbol{x}|0)\Delta\boldsymbol{C}^{-1} \cdot \boldsymbol{L}(0, \boldsymbol{x}^i)$$
$$: \boldsymbol{\varepsilon}^0(x_3^i)d\boldsymbol{x} \tag{14}$$

The particle probability function $P(\boldsymbol{x}|0)$ is also expanded with Taylor expansion to the first order to accommodate the gradation of particle distribution:

$$P(\boldsymbol{x}|0) = \frac{3}{4\pi a^3} \left[\phi(X_3) + e^{-\frac{x}{\delta}}\phi_{,3}(X_3) \cdot x_3\right] \tag{15}$$
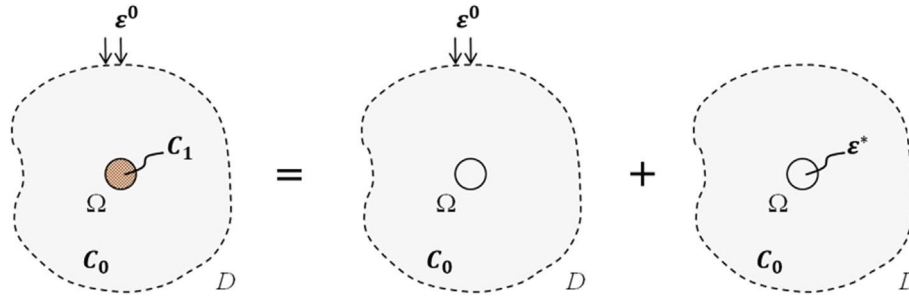
Fig. 2. Eshelby's equivalent inclusion method – using an eigenstrain in an inclusion to represent the inhomogeneity.
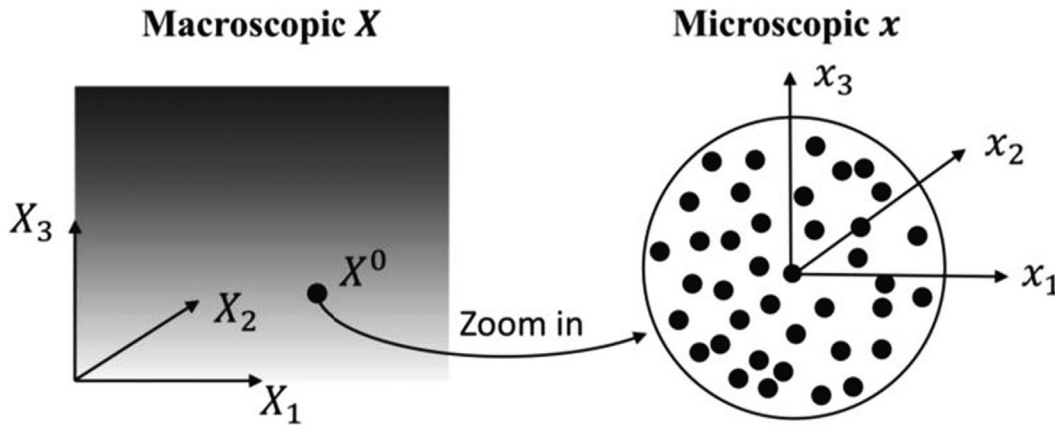

Fig. 3. A micromechanics-based model of FGM to predict the effective behavior considering the microstructural aspects.

The δ is the parameter to control the attenuation rate such that the probability function remains within a reasonable range inside the RVE, $\phi(X_3^0)$ is the average volume fraction of particle in the RVE and $\phi_{,3}(X_3^0)$ is the gradient of the particle volume fraction. Eqs. (13) to (15) are plugged into Eq. (12) such that the explicit relation between particle strain and prescribed far field strain is formulated:

$$\langle \boldsymbol{\varepsilon} \rangle (X_3) = \left(\boldsymbol{I} - \boldsymbol{D}^\Omega \cdot \Delta \boldsymbol{C} \right)^{-1} : \boldsymbol{\varepsilon}^0(X_3) + \phi \Delta \boldsymbol{C}^{-1} \cdot \mathcal{D}$$
$$: \varepsilon^0(X_3) + \phi_{,3} \Delta \boldsymbol{C}^{-1} \cdot \mathcal{F} : \boldsymbol{\varepsilon}_{,3}^0(X_3) \tag{16}$$

The definition and expression of $\mathcal{D}$ and $\mathcal{F}$ are introduced in the appendix Eqs. (A4) and (A5). Tensor $\mathcal{D}$ addresses the pairwise interaction between particles, while tensor $\mathcal{F}$ specially accounts for the coupling of layers along the gradation direction. Eq. (16) relates the ensemble average particle strain $\langle \boldsymbol{\varepsilon} \rangle (X_3)$ with its corresponding prescribed far field strain $\boldsymbol{\varepsilon}^0(X_3)$. It is straightforward to consider the prescribed far field strain $\boldsymbol{\varepsilon}^0$ as the matrix strain in macroscopic, after which the overall macroscopic stress $\overline{\boldsymbol{\sigma}}$ can be derived as the volumetric average of the particle stress and the matrix stress as:

$$\overline{\boldsymbol{\sigma}} = \phi(X_3)\boldsymbol{C}_1 : \langle \boldsymbol{\varepsilon} \rangle (X_3) + [1 - \phi(X_3)]\boldsymbol{C}_0 : \langle \boldsymbol{\varepsilon} \rangle^0(X_3) \tag{17}$$

Given $\overline{\boldsymbol{\sigma}}$, Eqs. (16) and (17) formulate an ordinary differential equation that can be solved by the backward Euler's method, such that the elastic behavior of FGMs considering the pairwise particle interaction is well defined.

It is noted that in the study of Yin et al (2004), three material zones like Phase-A particles with Phase-B matrix (Zone I), transition zone (Zone II) and Phase-B particles with Phase-A matrix (Zone III) are introduced to study the elastic properties of FGMs. In which, the volume fraction could cover 0%-100% by transferring the particle phase to matrix phase for Zone III and utilizing Zone II to bridge the results from Zone I and Zone III. However, since the FGMs used in the present study has less than 60% of the particle volume fraction (Chen and Yin, 2016), only one zone is considered in scope of this paper. Otherwise the HDPE, which serves as the binder to aluminum particles, is not enough to bind all the particles and will introduce significant air voids into the composite.

3. Effective plastic behavior of FGMs based on micromechanics

In this section, a brief review of plastic formulation of FGMs is given to introduce the background and to fulfill the insufficient derivation of our previous work (Lin et al., 2019). In the plastic analysis of two-phase FGMs (Lin et al., 2019), it is assumed that plasticity only occurs in the matrix phase, and the reinforcement stays completely elastic. If the volume fraction reaches more than 50%, the matrix and the reinforcement will switch and the plasticity no longer happens in the matrix, but inside the "reinforcement". The proposed theory will not hold for this scenario, and additional research work is needed to address this issue. The pressure-sensitive behavior of HDPE (Seltzer et al., 2011) is neglected for simplicity in this paper. It is worth noting that the derivation is based on Cauchy strain theory. For large plastic deformation (Ayoub et al., 2010), quadratic terms are needed in the strain definition. Thus, von Mises associated yield rule with isotropic hardening is considered (Simo and Hughes, 2006):

$$F(\boldsymbol{\sigma}, e^p) = \sqrt{H} - \sqrt{\frac{2}{3}} K(e^p) \tag{18}$$

For an isotropic homogeneous material, the stress norm takes the form $H = \boldsymbol{\sigma} : \boldsymbol{I_d} : \boldsymbol{\sigma}$, and the isotropic hardening function takes the form $K(e^p) = \sigma_Y + h(e^p)^q$, where σ_Y is the yield stress, h and q

are the hardening parameters and e^p is the effective plastic strain. However, such stress norm definition is suitable for isotropic homogeneous material and can only be applied to the matrix in the microscopic scale. The local disturbance from the particle inhomogeneity plays a key role in determining the starting place of the plastic deformation and the corresponding plastic strain rate. In order to incorporate the microscopic effect, the philosophy of the ensemble average method in Section 2 is used in the plastic analysis of FGMs, to convert the particles' interaction in microscope to the averaged relation in macroscope, such that both particle to matrix influence and the particle to particle pair-wise interactions are characterized. Since the stress/strain relationship obtained is at the macroscopic scale while the traditional von Mises stress is defined for the matrix phase in the microscopic scale, an ensemble average form of the current stress norm $\langle H \rangle$, is defined following Ju and Chen (1994c), and the corresponding effective yield function are used to define the macroscopic behavior. Based on that, the ensemble averaged form of $\langle H \rangle$ is defined as (Ju and Chen, 1994c):

$$\sqrt{\langle H \rangle} = (1 - \phi)\sqrt{\langle H \rangle_m} \tag{19}$$

where, $\langle H \rangle_m$ stands for the ensemble average form of $\langle H \rangle$ in the matrix phase. Since no plastic deformation is allowed in the elastic particles, the ensemble average of $\langle H \rangle$ in the particle phase is neglected, which is different from our previous work (Lin et al., 2019) and make the model more sufficient. It is noted that the hardening only occurs in matrix phase and has no contribution from particle phase, therefore the e^p in Eq. (18) is replaced with the matrix effective plastic strain e_m^p. The ensemble average yield function $\overline{F}$ for two-phase FGMs is written as:

$$\overline{F}(\sigma, e_m^p) = (1 - \phi)\sqrt{\langle H \rangle_m} - \sqrt{\frac{2}{3}}K(e_m^p) \tag{20}$$

Given a particle configuration $\mathcal{G}$, the ensemble average stress norm of matrix is defined as:

$$\langle H \rangle_m(\boldsymbol{x}) = H^0 + \int_g \left\{ H(\boldsymbol{x}|\mathcal{G}) - H^0 \right\} P(\mathcal{G}) d\mathcal{G} \tag{21}$$

where $H^0 = \sigma^0 : \boldsymbol{I_d} : \sigma^0$ stands for the macroscopic average of current stress norm of matrix and the second term represents the integration of the microscopic variation due to particle interaction over the entire representative volume element. The evaluation based on real particle configuration $\mathcal{G}$ is impossible. The higher order effect of particle influence in Eq. (21) is neglected, leaving only the first order influence of particle to matrix, to have a simplified ensemble average stress norm of the matrix phase:

$$\langle H \rangle_m(\boldsymbol{x}) = H^0 + \int_{|\boldsymbol{x}-\boldsymbol{x}_1|>a} \left\{ H(\boldsymbol{x}|\boldsymbol{x}_1) - H^0 \right\} P(\boldsymbol{x}_1) d\boldsymbol{x}_1 \tag{22}$$

where $P(\boldsymbol{x}_1)$ is the probability density function with the same form as Eq. (15). With the help of Eqs. (1), (2) and (4), the matrix stress is evaluated as:

$$\sigma = \sigma^0 + \sigma' = (\boldsymbol{I} + \boldsymbol{A}) : \sigma^0 \tag{23}$$

where $\boldsymbol{A} = -\boldsymbol{D}(\boldsymbol{x}) : \left(\boldsymbol{D}^\Omega - \Delta \boldsymbol{C}^{-1} \right)^{-1}$. Substituting Eq. (23) into Eq. (22) yields the explicit form of ensemble average stress norm of matrix as follows:

$$\langle H \rangle_m(\boldsymbol{x}) = H^0 + \int_{|\boldsymbol{x}-\boldsymbol{x}_1|>a} \left\{ \overline{\boldsymbol{A}} : \boldsymbol{I_d} : \boldsymbol{A} + \overline{\boldsymbol{A}} : \boldsymbol{I_d} + \boldsymbol{I_d} : \boldsymbol{A} \right\} P(\boldsymbol{x}_1) d\boldsymbol{x}_1$$
$$= \sigma^0 : \boldsymbol{T}^0 : \sigma^0 \tag{24}$$

where $\overline{\boldsymbol{A}} = -\left(\boldsymbol{D}^\Omega - \Delta \boldsymbol{C}^{-1} \right)^{-1} : \boldsymbol{D}(\boldsymbol{x})$, and the components of the fourth rank tensor $\boldsymbol{T}^0$ are given by

$$T_{ijkl}^0 = T_1^0 \delta_{ij}\delta_{kl} + T_2^0 \left(\delta_{ik}\delta_{jl} + \delta_{il}\delta_{jk} \right) \tag{25}$$

where

$$3T_1^0 + 2T_2^0 = \frac{(3\alpha + 2\beta)^2(1 - 2v_0)^2\phi}{18(1 - v_0)^2\mu_0^2} \tag{26}$$

$$T_2^0 = \frac{1}{2} + \frac{\phi(23 - 50v_0 + 35v_0^2)\beta^2}{225(1 - v_0)^2\mu_0^2} \tag{27}$$

and α and β are given in the appendix Eq. (A10d), which give a respond to Lin et al. (2019) μ_0 and v_0 are the shear modulus and Poisson's ratio of matrix, respectively. It is noted that the first order term of probability density function Eq. (15) vanishes, thanks to the symmetry of the volume integral. The probability density function can also be expanded to higher order term to account for larger gradation of particle volume fraction, which will generate additional terms in Eq. (24).

Eq. (24) gives the stress norm that accounts for the first order particle–matrix influence. It assumes dilute particle configuration so that the disturbed strain field from each particle can be linearly superposed. The pairwise particle interaction shall be considered when the volume fraction is high. It is seen that Eq. (16) and (17) give the relation between the ensemble average stress $\overline{\sigma}$ and the macroscopic matrix stress σ^0:

$$\sigma^0 = \boldsymbol{P} : \overline{\sigma} \tag{28}$$

However, the derivative of far field strain ε_3^0 in Eq. (16) makes the fourth rank tensor $\boldsymbol{P}$ implicit, where the backward Euler's method shall be used to numerically determine the $\boldsymbol{P}$ in each layer along the gradation. Since Eq. (28) holds for each individual layer $(\sigma^0)^i = \boldsymbol{P}^i : (\overline{\sigma})^i$, we have:

$$(\overline{\sigma})^i = \boldsymbol{H} : (\sigma^0)^i + \boldsymbol{Q} : (\sigma^0)^{i-1} \tag{29}$$

where i denotes the ith layer along the thickness, and

$$\boldsymbol{H} = \left\{ \phi\boldsymbol{C}_1 \cdot \left[\left(\boldsymbol{I} - \boldsymbol{D}^\Omega \cdot \Delta \boldsymbol{C} \right)^{-1} + \phi\Delta\boldsymbol{C}^{-1} \cdot \mathcal{D} \right] \cdot \boldsymbol{C}_0^{-1} + (1 - \phi)\boldsymbol{I} \right\}$$
$$- \boldsymbol{Q} \tag{30}$$

$$\boldsymbol{Q} = -\frac{N}{t} \phi_{,3} \phi\boldsymbol{C}_1 \cdot \Delta\boldsymbol{C}^{-1} \cdot \mathcal{F} \cdot \boldsymbol{C}_0^{-1} \tag{31}$$

in which t is the thickness and N denotes the number of layers along gradation. Since the load is transferred along gradation, the ensemble average stresses are the same in each layer $(\overline{\sigma})^i = (\overline{\sigma})^j$. Therefore, the relation between different $\boldsymbol{P}^i$ is given as:

$$\boldsymbol{I} = \boldsymbol{H} : \boldsymbol{P}^i + \boldsymbol{Q} : \boldsymbol{P}^{i-1} \tag{32}$$

The boundary at $i = 1$ corresponds to the 100% matrix material, such that an explicit equation can be formulated by Eqs. (16) and (17) to calculate $\boldsymbol{P}^0$. For the FGMs of which the particle volume fraction does not start from 0% (say 10%), the boundary condition can be formulated by dropping the $\boldsymbol{Q}$ term in Eq. (29), such the gradation effect is neglected in the first layer.

Compared with Eq. (24), the new stress norm in terms of ensemble average stress also varies along gradation and is written as:

$$\langle \boldsymbol{H} \rangle_m^i(\boldsymbol{x}) = \overline{\sigma} : \overline{\boldsymbol{T}}^i : \overline{\sigma} \tag{33}$$

where the fourth order tensor $\overline{\boldsymbol{T}}^i$ is defined as:

$$\overline{\boldsymbol{T}}^i = \boldsymbol{P}^i : \boldsymbol{T}^0 : \boldsymbol{P}^i \tag{34}$$

Therefore, the yield function for FGMs becomes:

$$\overline{F}^i\left(\overline{\boldsymbol{\sigma}}, e_m^p\right) = (1-\phi)\sqrt{\overline{\boldsymbol{\sigma}} : \overline{\boldsymbol{T}}^i : \overline{\boldsymbol{\sigma}}} - \left[\sigma_Y + h\left(e_m^{p\,i}\right)^q\right] \tag{35}$$

Following the associative flow rule, the macroscopic plastic strain in each layer is determined by:

$$\dot{\overline{\boldsymbol{\varepsilon}}}^p = \dot{\lambda}\frac{\partial \overline{\boldsymbol{F}}}{\partial \overline{\boldsymbol{\sigma}}} = \dot{\lambda}(1-\phi)\frac{\overline{\boldsymbol{T}} : \overline{\boldsymbol{\sigma}}}{\sqrt{\overline{\boldsymbol{\sigma}} : \overline{\boldsymbol{T}} : \overline{\boldsymbol{\sigma}}}} \tag{36}$$

Accordingly, the effective plastic strain for the matrix is:

$$\dot{e}_m^p = \frac{\dot{e}^p}{1-\phi} = \frac{1}{1-\phi}\sqrt{\frac{2}{3}\dot{\overline{\boldsymbol{\varepsilon}}}^p : \dot{\overline{\boldsymbol{\varepsilon}}}^p} \tag{37}$$

The macroscopic total strain is the volumetric average of the particle and matrix as:

$$\langle \boldsymbol{\varepsilon} \rangle = (1-\phi)\boldsymbol{\varepsilon}_m + \phi\boldsymbol{\varepsilon}_p \tag{38}$$

where the matrix strain is the combination of its elastic and plastic part $\boldsymbol{\varepsilon}_m = \boldsymbol{\varepsilon}_m^e + \boldsymbol{\varepsilon}_m^p$, and the total strain of particle only contains elastic part $\boldsymbol{\varepsilon}_p = \boldsymbol{\varepsilon}_p^e$. The elastic part $\boldsymbol{\varepsilon}_m^e$ and $\boldsymbol{\varepsilon}_p^e$ are determined with the help of elastic algorithm described in the section 2.2, while the plastic part $\boldsymbol{\varepsilon}_m^p$ is fully defined by Eqs. (35) to (37).

If the macroscopic ensemble average stress $\overline{\boldsymbol{\sigma}}$ is known, the consistency condition requires the yield function Eq. (28) smaller or equal to zero, which determines the effective plastic strain directly. In case of the strain-driven plasticity, return mapping algorithm is applied to perform the stress update, during which Newton's method or Bisection can be used to determine the $\dot{\lambda}$ from consistency condition. Specifically, in each loading step the trial stress in every layer $(\Delta\sigma^{tr})^i$ corresponding to the loading step ΔF is computed via the elastic algorithm in Section 2.2, which is plugged into Eq. (35) to see if the consistency condition holds based on the parameters in the previous loading step:

$$\overline{F}^i\left(\overline{\boldsymbol{\sigma}}, e_m^p\right) = (1-\phi)\sqrt{\overline{\boldsymbol{\sigma}} : \overline{\boldsymbol{T}}^i : \overline{\boldsymbol{\sigma}}} - \left[\sigma_Y + h\left(e_m^{p\,i}\right)^q\right] \leq 0 \tag{39}$$

If consistency condition holds true in every layer, then the FGM stays the elastic state or plastic unloading. If the yield function is larger than zero in a layer, $\overline{F}^i(\overline{\boldsymbol{\sigma}}, e_m^p) > 0$, then plastic strain occurs and the material parameters need to be updated, where the discrete form of Eqs. (36) and (37) are plugged into consistency condition to solve for the $\dot{\lambda}$ with the Newton's method or the bisection method.

4. Verification and validation

4.1. Verification: Uniaxial compression of PRMMC

In order to prove the accuracy of the proposed method, comparisons to existing methodology and experiments are needed for the verification purpose. However, to the best of the author's knowledge, neither theoretical modeling nor experimental data has been documented for the elastoplastic behavior of FGMs. The plastic behavior of particle-reinforced metal matrix composites (PRMMC), however, has been well documented and studied. PRMMCs are widely used as they can exhibit nearly isotropic properties and are easier to process using standard metallurgical processing such as powder metallurgy or casting routes. The reinforcing particles are assumed to be uniformly distributed among the metal matrix to exhibit an overall homogeneous mechanical behavior, which can be considered a special case of functionally graded material with constant particle volume fraction along the gradation. Therefore, the proposed method is downgraded to compare with the experimental data and theoretical model of PRMMC for verification. Specifically, experiments conducted by Yang et al. (1991) are used as a reference. Micromechanics based elastoplastic behav-

ior algorithm of PRMMC in the paper of Ju and Chen (1994c) is also compared for the verification. Notice that the proposed method shares the same framework with Ju's method, in which the particle interaction in both methods is addressed through the equivalent inclusion method. However, the effect of neighboring particles is addressed in different ways in two methods, whereas the pairwise interaction term in the present method is derived from physics in a more straightforward way and is easier to utilize for FGM modeling. In the experiment, uniaxial loading is applied to the Al/4Mg alloy reinforced with SiC particles, where the material properties for the matrix is $E_0 = 75\mathrm{GPa}$, $v_0 = 0.33$ and for the particle $E_1 = 420\mathrm{GPa}$, $v_1 = 0.17$. The hardening parameters for the matrix is given as $\sigma_Y = 46\mathrm{MPa}$, $h = 320\mathrm{MPa}$ and $q = 0.265$. Four types of particle volume fractions $\phi = 0\%, 17\%, 30\%$ and 48% are investigated. Since the macroscopic ensemble average stress equals to the applied stress and is known $\overline{\boldsymbol{\sigma}} = (\overline{\sigma}_{11}, 0, 0, 0, 0, 0)$. The effective plastic strain e_m^p can be directed computed from Eq. (35). The total strain can be fully determined with the help of Eqs. (16), (17), (36) and (38). Yang's experimental results, Ju's theoretical predictions and the prediction of the proposed algorithm are plotted in Fig. 4 for comparison. The solid line is the theoretical prediction based on present theory, the triangles represent the result from Ju and Chen's (1994c) theoretical prediction and the circular dots are the experimental result from Yang's experiment.

Very good agreement is achieved among the proposed theory, Ju and Chen's (1994c) theory and the experiment for PRMMC. The minor deviations between experiments and simulations at 30% may be attributed to the influence of residual stresses, which is caused by the reduction of the flow strength (Yang et al., 1991). In general, the proposed theory slightly underestimates the total deformation compared with Ju's results, but perfectly captures the experiment deformation when $\phi = 48\%$. It is noted that both Ju's theory and the present theory share the same fundamental derivation. The small discrepancy is resulted from the different formulation of pairwise interaction effect to the definition of microscopic stress field and ensemble average stress norm, where a more straightforward calculation is achieved in the present theory.

4.2. Validation: Uniaxial compression of FGMs

The experimental validation is conducted by comparing to the FGM from our recent research works (Yin et al., 2013; Chen et al., 2016; Chen and Yin, 2016) by developing a BIPVT roofing panel with FGMs as an essential component, which have shown great potential to harvest solar energy efficiency. The FGMs were made by coarse aluminum powder and HDPE through the vibration method. Coarse aluminum powder (Al-111) was chosen to mix with the finer HDPE powder. The desired gradation of the Al/HDPE FGM in terms of volume fraction of aluminum to the FGM is to be from 0% to 50% across its thickness. Aiming at this gradation, a mixing design of the FGM with an appropriate volume ratio of Al to HDPE as 1:3 was applied and the ethanol added for the mixing was chosen by the weight ratio of ethanol to the mixed powder as 28%. The detailed mix design and fabrication processes are provided in reference (Chen et al., 2016). HDPE by its nature exhibits viscous and thermoplastic behavior at higher temperatures, such that temperature and time have strong effect in its overall behavior under long time loading. However, those effects are neglected during the current validation process, thanks to the relatively short loading period and stable room temperature during the uniaxial compression tests. Potential thermal residual stress does exist from the temperature decrease during the manufacturing but is neglected for simplicity. The uniaxial compression test is carried out to validate the proposed theory developed from classical elastoplastic scenario based on the von Mises yielding criteria.
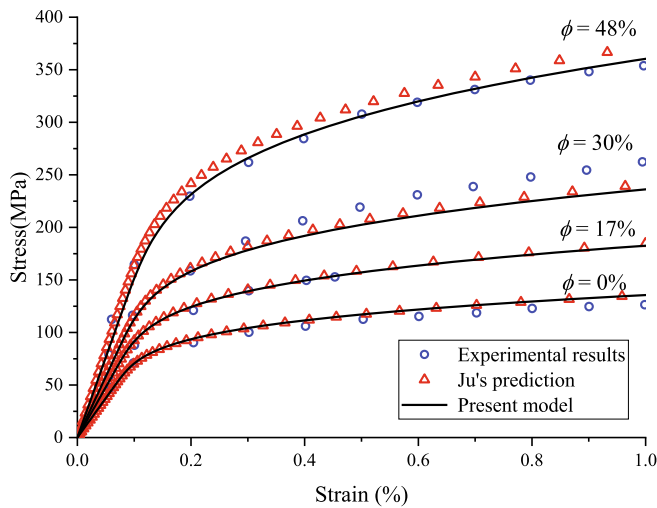
Fig. 4. Theoretical prediction and experimental data of plastic deformation of uniaxial compression of PRMMC.
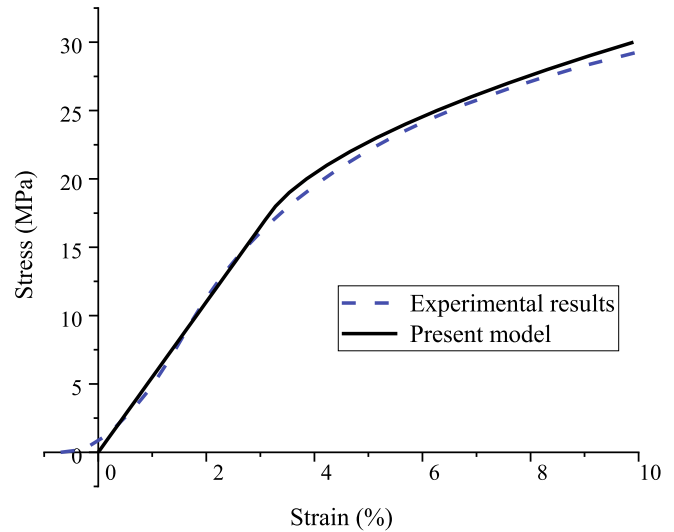

Fig. 5. Elastoplastic behavior of pure HDPE under uniaxial loading.

The uniaxial elastoplastic compression test is conducted with pure HDPE samples and the stress strain loading curve is shown in Fig. 5. It is worth noting that the derivation is based on Cauchy strain theory. For large plastic deformation (Ayoub et al., 2010), quadratic terms are needed in the strain definition. The curve is switched leftward to account for effect unflatten and unparalleled loading surface to the linear elastic behavior of HDPE. The material properties are extracted from the loading curve, such that $E = 550MPa, v = 0.3, \sigma_Y = 17.6MPa, h = 67.5MPa, q = 0.5444$. The corresponding restored loading curve is also plotted in Fig. 5, which matches well with the experimental data of HDPE and will be used in the following analysis of the composites.

Four samples are cut from an FGM plate for the uniaxial compression test, with its dimension and weight information listed in Table 1. The samples are uniaxially compressed with the Instron 5984 34 k Universal Testing Machine inside the Carleton Laboratory of Columbia University and all samples are kept under constant temperature and humidity environment. In order to clarify the region of interest (ROI) of the samples, two assumptions are introduced: a). there is a particle right at the center of the ROI, so that the interaction between particles can be established; b). the particle distribution follows the volume fraction distribution in the graded direction (x_3 in microscope), and follows uniform distribution in the other two direction (x_1 and x_2 in microscope). The samples are loaded with the speed of 0.508 mm/min until 1.524 mm total deformation is reached, where the approximate total deformation is about 10%. A high-resolution photo is taken at the beginning of each loading test, with Canon DSLR 6D camera and the Tamron 90 mm f/2.8 macro lens. The YongNuo YN-14EX macro flash light is mounted onto the Tamron macro lens to provide additional light in the macro photographing. The experiment setup is shown in Fig. 6(a). The macro lens allows a much closer shooting distance such that the frame can be filled as much as possible by the small FGM sample to reveal more detail of the FGM cross section, as can be seen from Fig. 6(b), where approximated 4 million effective pixels are included in the area of the 161.29 mm^2 cross-section surface. The cross-section photos are used to statistically retrieve the particle volume fraction distribution through the image analysis.

In Chen et al (2016), the particle volume fraction was measured. The samples were taken from the four corners and the center of the FGM plate after sedimentation and before heating and vacuuming inside the oven. Four layers were divided along the gradation and mixed together according to their relative position. The average volume fraction in the four mixed parts were measured and plotted. The corresponding simulated particle volume fraction starts with 0% at one end and linearly increase to 50% to the other end. However, the heating and vacuuming process will surely change the particle distribution along gradation, and thus cannot be assume linear as the particle volume fraction distribution plays vital role in the plastic behavior prediction. In order to get an accurate and individualized particle distribution, image-based analysis method is proposed and validated in this paper.

It is assumed that the particle volume fraction varies only along the gradation direction and stays unchanged over the horizontal plane. Statistically speaking, the particle volume fraction distribution of a sample can represent the distribution of all other samples and can also be represented by the volume fraction distribution shown in the cross section in Fig. 6(b), by counting the relative area of aluminum to the overall sample surface. Recognition of aluminum particles' area is accomplished by image analysis. Aluminum shows a high reflection rate to the flashed light, while HDPE, as a plastic, absorbs most of the light from the flash and shows relatively much darker in the Fig. 6 (b), making it easy to be distinguished. It shall be noted that HDPE is partially transparent, which means the aluminum particles in deeper layer will show up in flash-disabled photos and may reduce the efficiency of the recognition. Therefore, the flash light greatly contributes to the differentiation of Al and HDPE by making the aluminum particle "shine" in the photo. This phenomenon also helps the surface Al to gain a much brighter color than the HDPE and stand out from the surrounding HDPE, as is shown in Fig. 7. A very clear and growing trend of the pixels close to 1 (indicating Al) can be observed from the top to the bottom.

Specifically, the captured image is first converted from RGB to the gray scale, where each pixel location has a number ranging from 0 to 1, representing the relative light intensity. The FGM sample is cropped from the whole photo and divided into 10 sections along the gradation. The histogram in each section is plotted in Fig. 7, where the upper left to the bottom right represent the top section to the bottom, correspondingly. The gray scale light intensity from 0 to 1 is divided into 100 sections. The histogram counts the number of occurrences of a certain light intensity range in the corresponding section. It is clearly seen that from top to bottom, the number of occurrences of brighter pixels (pixel information close to 1) increase along gradation, in accordance with the gradual increase of aluminum particle volume fraction.
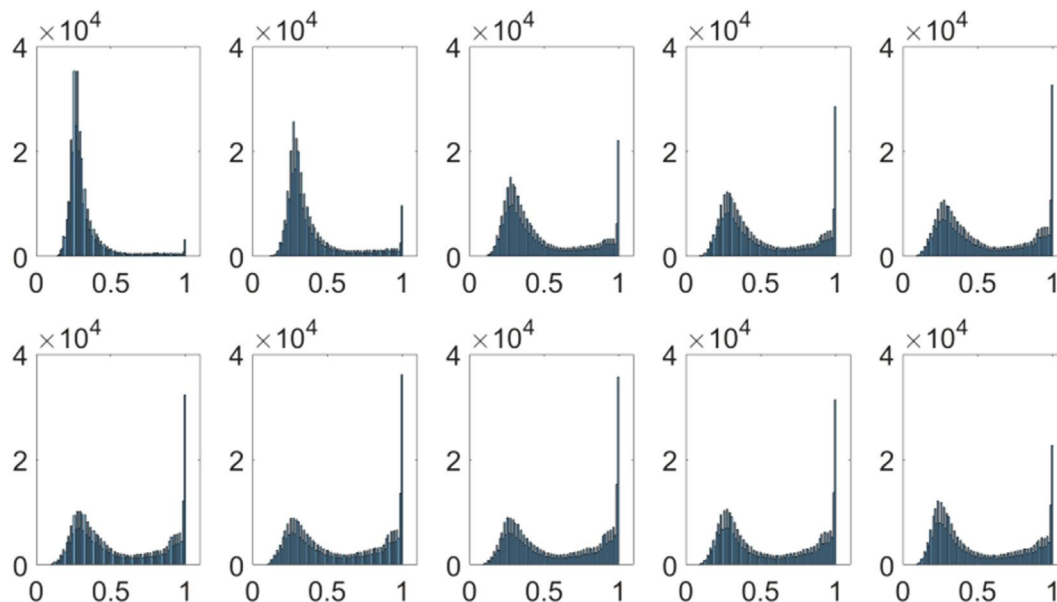
Table 1
The dimension and weight information of the FGM samples.

Sample	Height	Width	Depth	Weight
#	mm	mm	mm	g
1	13.39	13.26	14.25	3.40
2	13.51	13.61	13.26	3.30
3	13.21	13.18	13.34	3.16
4	13.64	13.74	13.61	3.43
Average	13.44	13.45	13.61	3.32
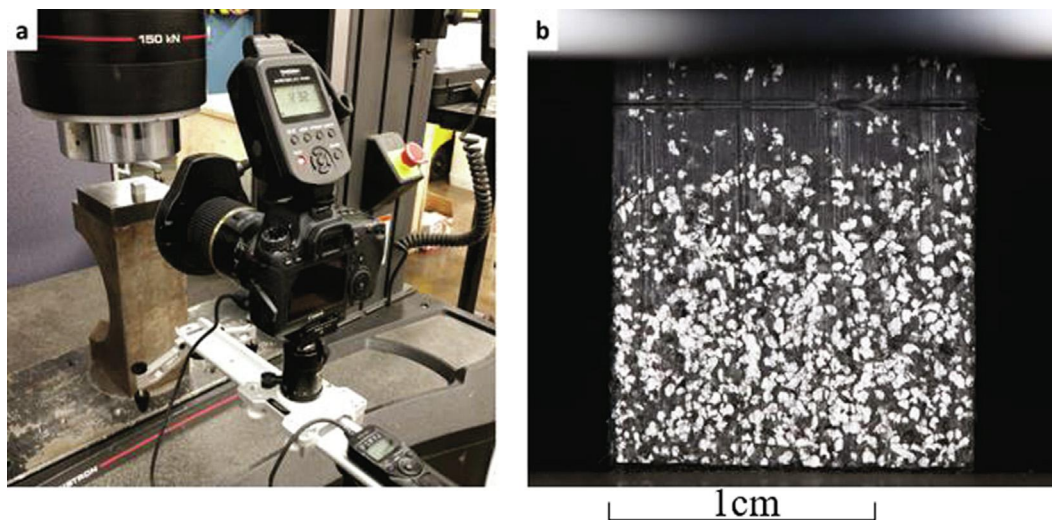
Fig. 6. Microstructure acquisition: (a). Experimental setup; (b). Macro photo of the FGM sample's cross section.

Fig. 7. The histograms along the gradation of the FGM sample in the 10 different sections along the gradation.

A light intensity threshold is settled to distinguish aluminum pixels from HDPE pixels, which is determined by calibrating the predicted weight of the sample to the measured ones. The porosity is not considered during this process, i.e. assuming no air void inside, because the sample is very cut into very small size and visually examined with no defects. Let us first assume that the light intensity threshold is set as 0.86, such that any pixel's light intensity larger than or equal to 0.86 is considered as part of aluminum particle, while smaller than 0.86 is considered as HDPE. The identification of aluminum or HDPE can thus be easily accomplished. The comparison of original image and Al-recognized image is shown in Fig. 8, where the red dashed line and the blue dashed mark are used to indicate the corresponding location of one Al particles and part of the HDPE matrix. It is seen that all the aluminum particles in the original photo are successfully recognized, while the vertical scratches from the sample-cutting and the aluminum particles hidden in deeper layer are filtered out.
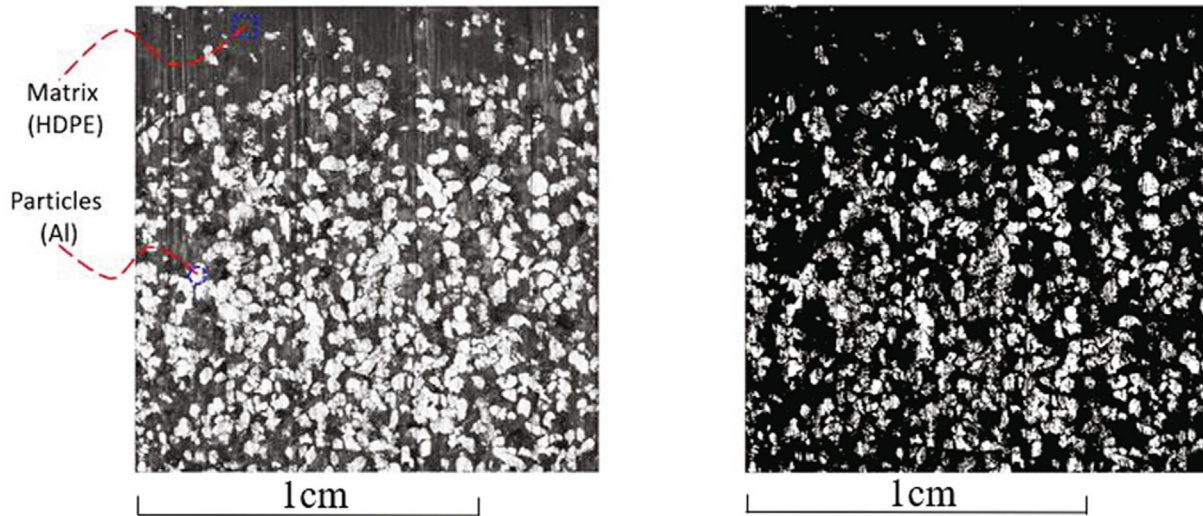
Fig. 8. FGM sample original photo (left) and Al-recognized photo (right).

Ten layers are divided along the gradation and the corresponding particle volume fraction is calculated by dividing the number of bright pixels to the total number of pixels. Such image analysis is repeated for all four FGM samples and the averaged particle volume fraction distribution is plotted in Fig. 9. The blue dots represent the averaged volume fraction, where the uncertainty is 0.07. A quadratic function with forced zero interception is used to fit the volume fraction distribution. The area below the fitted curve is the averaged particle volume fraction. Given the sample dimension in Table 1, the weight corresponding to the averaged volume fraction is calculated as 3.31 g, which matches well with the measured average sample weight 3.32 g, where the uncertainty of the average sample weight is 0.16 g, such that the light intensity threshold 0.86 is validated. It is seen from Fig. 9 that when the relative location is smaller than 0.6, the particle volume fraction gradually increases in convex form until approximately 30% and gradually stabilize with a slight decrease. The retrieved averaged sample particle volume fraction distribution is slightly different with the linear distribution assumption in the paper of Chen et al (2016). The decrease of the volume fraction is due to the boundary effect of the mold. The gradation is resulted from a sedimentation process, where the mold containing the sample solution is fixed to a shaking table with vertical vibration. Since the bottom surface is fixed to the shaking table, the particles close to the bottom surface are forced to bounce back, and therefore the bottom layer is formulated with less particles. The layer close to the bottom will accumulate both the particles fallen from the top and the particles bounced back from the bottom, and therefore has the largest volume fraction across the thickness.

Uniaxial compression test is applied to all the FGM samples, until the total deformation reaches around 10%. The stress–strain curve of experimental results and numerical results are plotted in Fig. 10. The experimental results of all samples are in dot marker with the error bar represents the maximum deviation of all samples. Numerical results with sample particle distribution given in Fig. 9, quadratic distribution and linear distribution which proposed by Chen et al. (2016), are marked in solid line, dash line and dot-dash line, respectively. The numerical comparison between the prescribed load and experimental load is listed in Table 2. The relative difference is calculated by dividing the difference of the prescribed load and the experimental load by the experimental load.
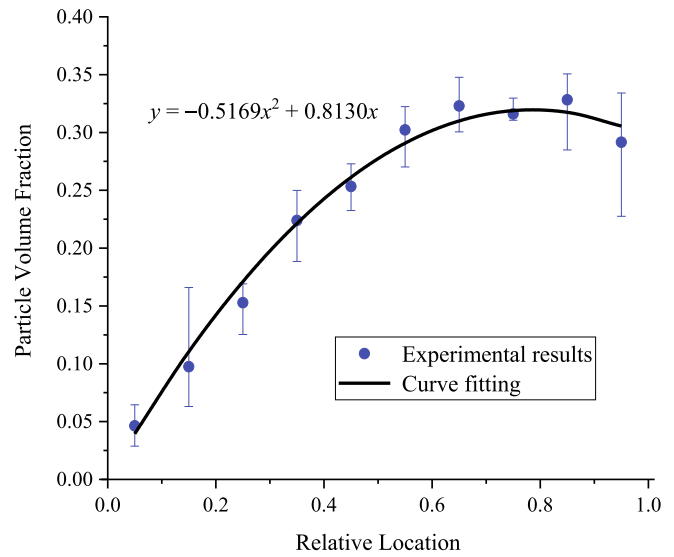

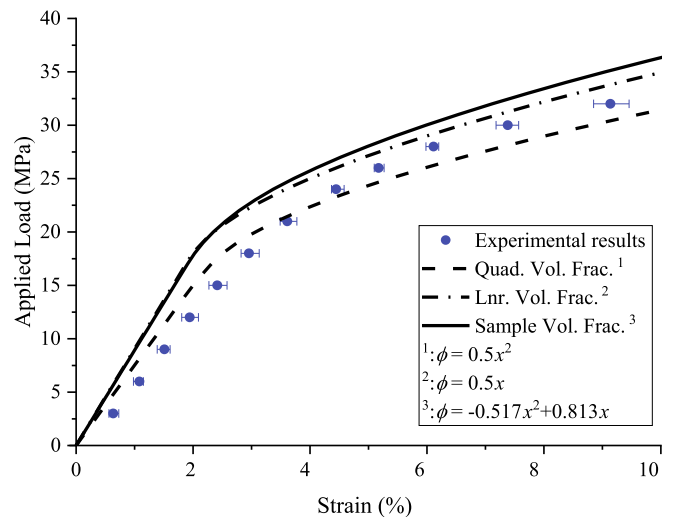**Fig. 9.** Aluminum volume fraction distribution in the gradation direction.

Fig. 10. Elastoplastic behavior of FGM in the experiments and prediction.

Table 2
Comparison between experiments and prescribed load of elastoplastic behavior of FGM, take the prescribed load as reference.

Strain %	Experiment Load MPa	Prescribed Load MPa	Relative Difference %	Strain %	Experiment Load MPa	Prescribed Load MPa	Relative Difference %
0.34	1.4	3.00	114.89%	3.37	19.98	24.00	20.13%
0.67	3.24	6.00	85.13%	4.1	22.86	26.00	13.71%
1.01	5.49	9.00	63.95%	4.98	25.37	28.00	10.37%
1.35	7.88	12.00	52.33%	5.98	27.76	30.00	8.07%
1.68	10.24	15.00	46.54%	7.12	29.64	32.00	7.97%
2.03	12.54	18.00	43.55%	8.38	31.22	34.00	8.90%
2.55	15.8	21.00	32.90%	9.05	31.93	35.00	9.62%

It is shown in Fig. 10 that the experimental data exhibit similar elastoplastic behavior with a narrow deviation over the whole loading process. The present theoretical elastoplastic prediction based on the true particle distribution tends to slightly underestimate the overall deformation but captures the trend of the behavior. The prediction mismatch happens majorly in the elastic domain and becomes not that obvious during the plastic stage. The maximum discrepancy happens at the beginning of the elastic loading and rapidly decreases when the deformation goes into plastic stage. According to best of the authors' knowledge, the discrepancy of prediction and experiment could be resulted from the following reasons. Firstly, the two phases are assumed to be perfectly bonded and free of defect like air void in theoretical framework. However, the connection between aluminum and HDPE may not be that strong. Moreover, although the manufacturing of the used FGM involves vacuuming process, air bubbles are still very likely to be trapped inside (Tan et al., 2005; Brassart et al., 2009), given the high viscosity of HDPE. Thirdly, the proposed algorithm is developed based on the assumption that the particle shape being spherical, which cannot be perfectly satisfied in the real case. Considering the overestimation of stiffness in the elastic range, the debonding and air void are very likely to dominate the causing for strong reduction of overall stiffness. It is worth to point out that the big initial percentage difference between prediction and experiments could also be resulted from the pressure dependency of HDPE. Overall, the proposed elastoplastic algorithm of FGM captures the real elastoplastic behavior of FGM very well and can be used for further investigation and industry prediction.

5. Parameter studies: The effect of volume fraction distributions

Volume fraction plays an important role on the FGM's properties. Based on the procedure mentioned above, when a uniaxial loading is applied to the Al/HDPE FGM, the effect of volume fraction distribution is studied in two cases: (1) different overall particle volume fractions with quadratic and linear distribution functions; (2) the same overall particle volume fraction with different quadratic distribution functions. In this section, the FGMs are assumed as a mixture of Al particles embedded in a HDPE matrix with maximum phase volume fraction remains smaller than 50%, to avoid the phase transition between particle and matrix. The mechanical parameters, which are $E_0 = 550\text{MPa}, v_0 = 0.3, \sigma_Y = 17.6\text{MPa}, h = 67.5\text{MPa}, q = 0.5444$ for HDPE matrix, and $E_1 = 70\text{GPa}, v_1 = 0.33$ for Al particles, are collected in Section 4. The effective Young's modulus E_e for the elastic behavior, the offset yield stress $\sigma_{0.2}$ and the corresponding total strain $\varepsilon_{0.2}$ for the plastic behavior are defined and calculated for comparison. The offset yield stress $\sigma_{0.2}$ is defined as the stress state corresponding to 0.2% plastic strain and has been used in many literatures (Barlat et al., 1991; Cleveland and Ghosh, 2002; Chowdhury et al., 2016; Samei et al., 2018) for the measurement of plastic behavior.

5.1. Effect of different volume fractions

Fig. 11 gives the elastoplastic predictions of FGMs under different overall particle volume fraction, with the quadratic and linear distribution function. The overall particle volume fraction ranges from 10% to 25%. The effective Young's modulus E_e, the offset yield stress $\sigma_{0.2}$ and the corresponding total strain $\varepsilon_{0.2}$ are listed in Tables 3 and 4 for comparison. It is seen that the effective Young's modulus E_e is strongly affected by the overall volume fraction, indicating that the overall volume fraction has a strong effect to the elastic behavior of the FGM. The effective Young's modules E_e will rise 1.95% with every 1% increase of the overall particle volume fraction. The offset yield stress $\sigma_{0.2}$ remain stable with variation smaller than 3% and can thus be considered as independent to the overall particle volume fraction. However, the corresponding
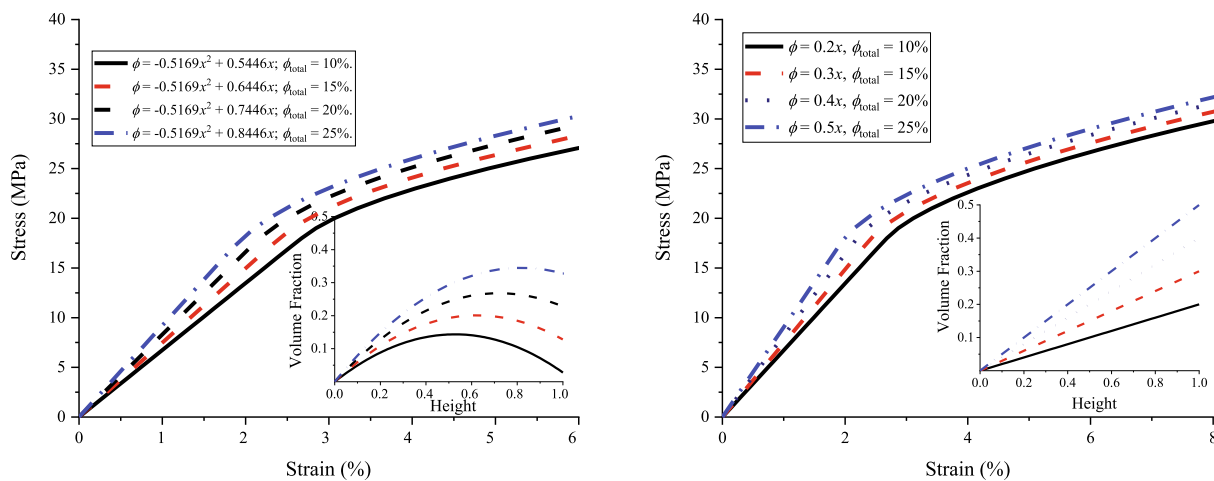
Fig. 11. Stress–strain curve of Al/HDPE composites of different overall particle volume fraction with quadratic distribution function (left) and linear distribution function (right).

Table 3

Comparison of E_e, $\sigma_{0.2}$ and $\varepsilon_{0.2}$ under different phase volume fractions with quadratic distribution, take volume fraction of 10% as reference, respectively.

Volume	E_e	Comparison	$\sigma_{0.2}$	Comparison	$\varepsilon_{0.2}$	Comparison
Fractions	MPa	–	MPa	–	%	–
10%	673.942	0.00%	20.607	0.00%	3.258	0.00%
15%	748.342	11.04%	20.936	1.60%	2.998	−7.98%
20%	830.767	23.27%	21.002	1.92%	2.728	−16.26%
25%	921.982	36.80%	20.835	1.11%	2.460	−24.49%

Table 4

Comparison of E_e, $\sigma_{0.2}$ and $\varepsilon_{0.2}$ under different phase volume fractions with linear distribution, take volume fraction of 10% as reference, respectively.
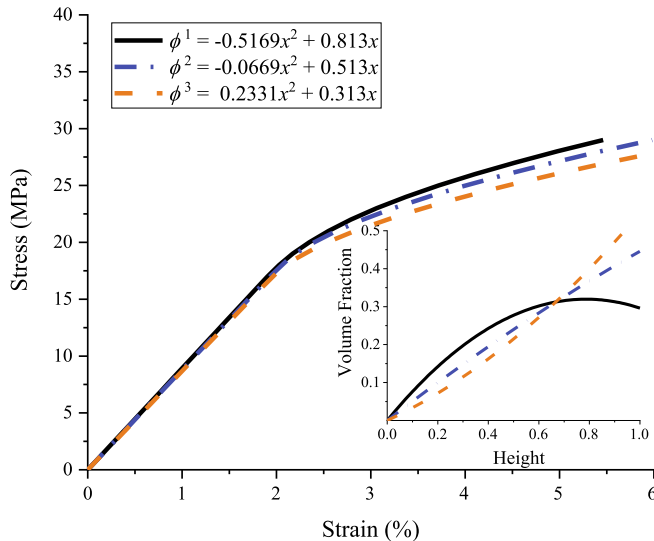
Volume	E_e	Comparison	$\sigma_{0.2}$	Comparison	$\varepsilon_{0.2}$	Comparison
Fractions	MPa	–	MPa	–	%	–
10%	671.9657	0.00%	20.2911	0.00%	3.21967	0.00%
15%	742.4855	10.49%	20.3984	0.53%	2.94731	−8.46%
20%	820.0698	22.04%	20.4014	0.54%	2.68777	−16.52%
25%	905.3679	34.73%	20.2798	−0.06%	2.43995	−24.22%

total strain $\varepsilon_{0.2}$ is significantly reduced to 40% with the increase of the overall stiffness. The difference between quadratic and linear distribution, under the same overall volume fraction, is less than 3% for all the three mechanical parameters. It is also worth mentioned that the prediction based on the linear particle distribution, given by Chen et al (2016) provides similar behavior prediction with the quadratic particle distribution and can be used as a simplified estimation of the particle distribution, from the elastoplastic perspective.

5.2. Effect of different quadratic distribution functions

In order to further study the effect of particle distribution function, Fig. 12 illustrates the elastoplastic predictions under the same overall particle volume fraction but different quadratic distribu-

Fig. 12. Stress–strain curve of Al/HDPE composites with different quadratic distributed function at the same overall particle volume fraction at 23.42%.

tions, which are listed in the legend. The overall particle volume fraction is equal to the measured result in the Section 4. The overall effective Young's modulus E_e, the overall offset yield stress $\sigma_{0.2}$ and the corresponding total strain $\varepsilon_{0.2}$ are listed in Table 5 for comparison. Since the overall particle volume fraction remains unchanged, and the particle distribution configuration is restricted to and varied from the authentic particle distribution formulation, the mechanical properties for both elastic and plastic stages are weakened with the increase of the gradation. The maximum difference is less than 3% for the effective Young's modulus E_e and about 6% for the offset yield stress $\sigma_{0.2}$. Together with the comparison in Section 5.1, it is therefore concluded that the slight variation in particle distribution function under the same overall volume fraction will not generate big difference in mechanical behaviors, as long as a similar trend is followed. However, for some extreme cases where particles are overly sedimented to formulate a delaminated composite, or insufficiently sedimented with almost homogeneous particle distribution along gradation, big difference in plastic deformation is expected and need further investigation.

6. Conclusions

The micromechanics-based algorithm to predict the elastoplastic behavior of FGMs is proposed in this paper. The pairwise interaction between particles is considered to account for the higher order effect from particle to matrix. The microscopic stress norm is transformed to the macroscopic stress norm for the yield function with ensemble average stress components. The coupling effect of neighboring layers is considered in the calculation of relation between ensemble average stress and far field stress, numerically through the backward Euler's method. The proposed algorithm is downgraded into homogeneous composite to compare with the elastoplastic algorithm (Ju and Chen, 1994c) and the uniaxial elastoplastic compression test (Yang et al., 1991) of particle reinforced metal matrix composites (PRMMC). The downgraded prediction agrees well with both theory and experiment.

Table 5

Comparison of E_e, $\sigma_{0.2}$ and $\varepsilon_{0.2}$ under different quadratic distributed functions, take ϕ^1 as reference, respectively.

Distribution	E_e	Comparison	$\sigma_{0.2}$	Comparison	$\varepsilon_{0.2}$	Comparison
Function	MPa	–	MPa	–	%	–
ϕ^1	892.16	0.00%	20.89	0.00%	2.542	0.00%
ϕ^2	880.00	−1.36%	20.45	−2.12%	2.524	−0.70%
ϕ^3	867.74	−2.74%	19.62	−6.11%	2.461	−3.19%

The uniaxial elastoplastic compression test of FGM is also conducted to validate the proposed algorithm. The image analysis method is proposed to statistically obtain the authentic particle volume particle distribution throughout the gradation. The elastoplastic behavior prediction based on the real particle distribution, linear distribution and quadratic distribution are discussed and compared with the experiment. The prediction based on the real particle distribution is in good agreement with the experiments but slightly underestimates the deformation, especially in the elastic range. The discrepancy in the elastic range may be due to the imperfect interface and potential debonding between particle and matrix and the potential defect (such as air void) inside the FGM samples. The spherical particle assumption may also contribute to the difference between prediction and experiments. It is also worth to point the pressure dependency of HDPE will also contribute to the discrepancy in the initial elastic loading. More future work is needed to further investigate the influence from potential thermal residual stress, viscous, thermoplastic and pressure dependency of HDPE for a more accurate prediction of the elastoplastic behavior of HDPE based FGMs.

The effect of overall volume fraction and particle distribution are numerically discussed. Cases with different overall particle volume fraction under specific type of distribution and different particles distribution under specific overall volume fraction are collected. The effective Young's modulus is strongly affected by the change of overall particle volume fraction in the thickness direction, but slightly affected by the particle distribution. The overall offset yield stress, however, is more affected by the distribution type than the overall particle volume fraction. Since only linear and quadratic distributions are considered, further study is needed to account for effect of extreme particle distributions, which are likely happened in the FGM manufacturing. Also, the mechanical properties of matrix and particles play important roles in FGM composites, which should be further studied to predict the overall effective elastoplastic behaviors of FGM composites with different configurations.

Declaration of Competing Interest

The authors declare that they have no known competing financial interests or personal relationships that could have appeared to influence the work reported in this paper.

Acknowledgement

Appendix

Integration of the modified Green's function in the matrix domain D_{ijkl}

$$D_{ijkl}(D_m) = D_1 n_i n_j n_k n_l + D_2\left(\delta_{ik}n_j n_l + \delta_{il}n_j n_k + \delta_{jk}n_i n_l + \delta_{jl}n_i n_k\right) \\ + D_3\delta_{ij}n_k n_l + D_4\delta_{kl}n_i n_j + D_5\delta_{ij}\delta_{kl} + D_6\left(\delta_{ik}\delta_{jl}+\delta_{il}\delta_{jk}\right)$$ (A1)

where

$$D_1 = \frac{\rho^3\left(5-7\rho^2\right)}{4\mu_0(1-v_0)}, D_2 = \frac{\rho^3\left(\rho^2-v_0\right)}{4\mu_0(1-v_0)}, D_3 = \frac{\rho^3\left(\rho^2-1\right)}{4\mu_0(1-v_0)}$$ (A2a)

$$D_4 = \frac{\rho^3\left(\rho^2-1\right)}{4\mu_0(1-v_0)}, D_5 = \frac{\rho^3\left(5-3\rho^2\right)}{60\mu_0(1-v_0)}, D_6 = \frac{\rho^3\left(-3\rho^2+10v_0-5\right)}{4\mu_0(1-v_0)}$$ (A2b)

The pairwise interaction tensor $L_{ijkl}(\boldsymbol{x}_1,\boldsymbol{x}_2)$

$$L_{ijkl}(L_m) = L_1 n_i n_j n_k n_l + L_2\left(\delta_{ik}n_j n_l + \delta_{il}n_j n_k + \delta_{jk}n_i n_l + \delta_{jl}n_i n_k\right) \\ + L_3\delta_{ij}n_k n_l + L_4\delta_{kl}n_i n_j + L_5\delta_{ij}\delta_{kl} + L_6\left(\delta_{ik}\delta_{jl}+\delta_{il}\delta_{jk}\right)$$ (A3)

where $L_i(i=1,2,\cdots,6)$ can be found in Yin's paper
The integration of the pairwise interaction tensor $\mathcal{D}$ and $\mathcal{F}$

$$D = \int_D \frac{3}{4\pi a^3}L(0,\boldsymbol{x})dx = \int_0^{\frac{1}{2}}\frac{3}{4\pi\rho^4}\int_\Sigma \boldsymbol{L}(\boldsymbol{n},\rho)d\omega d\rho$$ (A4)

$$F = \int_D e^{-\frac{x}{\delta}}\frac{3}{4\pi a^3}L(0,\boldsymbol{x})x_3^2 dx = \int_0^{\frac{1}{2}}e^{-\frac{a}{\rho_0}}\frac{3a^2}{4\pi\rho^6}\int_\Sigma \boldsymbol{L}(\boldsymbol{n},\rho)n_3^2 d\omega d\rho$$ (A5)

where

$$\int_\Sigma L(\boldsymbol{n},\rho)d\omega = \frac{4\pi}{15}(15L_5+10L_3+L_1)\delta_{ij}\delta_{kl} \\ + \frac{4\pi}{15}(15L_6+10L_2+L_1)\left(\delta_{ik}\delta_{jl}+\delta_{il}\delta_{jk}\right)$$ (A6)

$$\int_\Sigma L(\boldsymbol{n},\rho)n_3^2 d\omega = \frac{4\pi}{105}[35L_5+14L_3+L_1+2(7L_3+L_1)(\delta_{I3}+\delta_{K3})]\delta_{ij}\delta_{kl} \\ + \frac{4\pi}{105}\left[35L_6+14L_2+L_1+2(7L_2+L_1)\left(\delta_{I3}+\delta_{J3}\right)\right]\left(\delta_{ik}\delta_{jl}+\delta_{il}\delta_{jk}\right)$$ (A7)

The relation between disturb stress $\boldsymbol{\sigma}'$ and far field stress $\boldsymbol{\sigma}^0$, $\boldsymbol{\sigma}' = \boldsymbol{A}:\boldsymbol{\sigma}^0$

$$A = -D:\left(\boldsymbol{D}^\Omega - \Delta\boldsymbol{C}^{-1}\right)^{-1}$$ (A8)

$$A_{ijkl}(A_m) = A_1 n_i n_j n_k n_l + A_2\left(\delta_{ik}n_j n_l + \delta_{il}n_j n_k + \delta_{jk}n_i n_l + \delta_{jl}n_i n_k\right) \\ + A_3\delta_{ij}n_k n_l + A_4\delta_{kl}n_i n_j + A_5\delta_{ij}\delta_{kl} + A_6\left(\delta_{ik}\delta_{jl}+\delta_{il}\delta_{jk}\right)$$ (A9)

where

$$A_1 = \frac{\rho^3\beta\left(7\rho^2-5\right)}{2\mu_0(1-v_0)}, A_2 = \frac{\rho^3\beta\left(v_0-\rho^2\right)}{2\mu_0(1-v_0)}, A_3 = \frac{\rho^3\beta\left(1-\rho^2\right)}{2\mu_0(1-v_0)}$$ (A10a)

$$A_4 = \frac{\rho^3\beta\left(1-\rho^2\right)-\rho^3\alpha(1-2v_0)}{2\mu_0(1-v_0)}, A_5 = \frac{\rho^3\beta\left(3\rho^2-5\right)+\rho^3\alpha(5-10v_0)}{30\mu_0(1-v_0)}$$ (A10b)

$$A_6 = \frac{\rho^3\beta\left(5-10v_0+3\rho^2\right)}{30\mu_0(1-v_0)}$$ (A10c)

$$\alpha = \frac{-\alpha_0}{(3\alpha_0+2\beta_0)2\beta_0}, \beta = \frac{1}{4\beta_0}$$ (A10d)

$$\alpha_0 = \frac{1}{30\mu_0(1-v_0)}-\left(\frac{1}{9\Delta\kappa}-\frac{1}{6\Delta\mu}\right), \beta_0 = \frac{5v_0-4}{30\mu_0(1-v_0)}-\frac{1}{4\Delta\mu}$$

References

Aboudi, J., Pindera, M.-J., Arnold, S.M., 2003. Higher-order theory for periodic multiphase materials with inelastic phases. Int. J. Plast. 19, 805–847.

Aghababaei, R., Joshi, S.P., 2011. Grain size–inclusion size interaction in metal matrix composites using mechanism-based gradient crystal plasticity. Int. J. Solids Struct. 48, 2585–2594.

Agoras, M., Avazmohammadi, R., Castañeda, P.P., 2016. Incremental variational procedure for elasto-viscoplastic composites and application to polymer-and metal-matrix composites reinforced by spheroidal elastic particles. Int. J. Solids Struct. 97, 668–686.

Amirpour, M., Das, R., Bickerton, S., 2017. An elasto-plastic damage model for functionally graded plates with in-plane material properties variation: Material model and numerical implementation. Compos. Struct. 163, 331–341.

Ayoub, G., Zaïri, F., Naït-Abdelaziz, M., Gloaguen, J.M., 2010. Modelling large deformation behaviour under loading–unloading of semicrystalline polymers: Application to a high density polyethylene. Int. J. Plast. 26, 329–347.

Barai, P., Weng, G.J., 2011. A theory of plasticity for carbon nanotube reinforced composites. Int. J. Plast. 27, 539–559.

Barlat, F., Lege, D.J., Brem, J.C., 1991. A six-component yield function for anisotropic materials. Int. J. Plast. 7, 693–712.

Birman, V., Byrd, L.W., 2007. Modeling and analysis of functionally graded materials and structures. Appl. Mech. Rev. 60, 195–216.

Bouhamed, A., Jrad, H., Mars, J., Wali, M., Gamaoun, F., Dammak, F., 2019. Homogenization of elasto-plastic functionally graded material based on representative volume element: Application to incremental forming process. Int. J. Mech. Sci. 160, 412–420.

Brassart, L., Inglis, H.M., Delannay, L., Doghri, I., Geubelle, P.H., 2009. An extended Mori-Tanaka homogenization scheme for finite strain modeling of debonding in particle-reinforced elastomers. Comput. Mater. Sci. 45, 611–616.

Brassart, L., Stainier, L., Doghri, I., Delannay, L., 2012. Homogenization of elasto-(visco) plastic composites based on an incremental variational principle. Int. J. Plast. 36, 86–112.

Chen, F., Yin, H., 2016. Fabrication and laboratory-based performance testing of a building-integrated photovoltaic-thermal roofing panel. Appl. Energy 177, 271–284.

Chen, F.L., He, X., Yin, H.M., 2016. Manufacture and multi-physical characterization of aluminum/high-density polyethylene functionally graded materials for green energy building envelope applications. Energy Build. 116, 307–317.

Chen, Y., Ghosh, S., 2012. Micromechanical analysis of strain rate-dependent deformation and failure in composite microstructures under dynamic loading conditions. Int. J. Plast. 32–33, 218–247.

Chowdhury, P., Sehitoglu, H., Maier, H.J., Rateick, R., 2016. Strength prediction in NiCo alloys – The role of composition and nanotwins. Int. J. Plast. 79, 237–258.

Christensen, R.M., Lo, K.H., 1979. Solutions for effective shear properties in three phase sphere and cylinder models. J. Mech. Phys. Solids 27, 315–330.

Cleveland, R.M., Ghosh, A.K., 2002. Inelastic effects on springback in metals. Int. J. Plast. 18, 769–785.

Eshelby, J.D., 1959. The elastic field outside an ellipsoidal inclusion. Proc. R Soc. London A 252, 561–569.

Eshelby, J.D., 1957. The determination of the elastic field of an ellipsoidal inclusion, and related problems. Proc. R. Soc. London A 241, 376–396.

Gasik, M.M., 1998. Micromechanical modelling of functionally graded materials. Comput. Mater. Sci. 13, 42–55.

Hashin, Z., 1988. The differential scheme and its application to cracked materials. J. Mech. Phys. Solids 36, 719–734.

Hill, R., 1965. Continuum micro-mechanics of elastoplastic polycrystals. J. Mech. Phys. Solids 13, 89–101.

Jrad, H., Mars, J., Wali, M., Dammak, F., 2018. An extended finite element method for modeling elastoplastic FGM plate-shell type structures. Struct. Eng. Mech. 68, 299–312.

Ju, J.W., Chen, T.M., 1994a. Micromechanics and effective moduli of elastic composites containing randomly dispersed ellipsoidal inhomogeneities. Acta Mech. 103, 103–121.

Ju, J.W., Chen, T.M., 1994b. Effective elastic moduli of two-phase composites containing randomly dispersed spherical inhomogeneities. Acta Mech. 103, 123–144.

Ju, J.W., Chen, T.-M., 1994c. Micromechanics and effective elastoplastic behavior of two-phase metal matrix composites. J. Eng. Mater. Technol. 116, 310–318.

Ju, J.W., Sun, L.Z., 2001. Effective elastoplastic behavior of metal matrix composites containing randomly located aligned spheroidal inhomogeneities. Part I: micromechanics-based formulation. Int. J. Solids Struct. 38, 183–201.

Ju, J.W., Tseng, K.H., 1997. Effective elastoplastic algorithms for ductile matrix composites. J. Eng. Mech. 123, 260–266.

Ju, J.W., Tseng, K.H., 1996. Effective elastoplastic behavior of two-phase ductile matrix composites: a micromechanical framework. Int. J. Solids Struct. 33, 4267–4291.

Koizumi, M., 1997. FGM activities in Japan. Compos. Part B Eng. 28, 1–4.

Kumar, V., Dutta, D., 1998. An approach to modeling & representation of heterogeneous objects. J. Mech. Des. 120, 659–667.

Kurimoto, M., Kato, K., Hanai, M., Hoshina, Y., Takei, M., Okubo, H., 2010. Application of functionally graded material for reducing electric field on electrode and spacer interface. Gas 1, 2.

Lahellec, N., Suquet, P., 2013. Effective response and field statistics in elasto-plastic and elasto-viscoplastic composites under radial and non-radial loadings. Int. J. Plast. 42, 1–30.

Li, J., Weng, G.J., 2007. A secant-viscosity composite model for the strain-rate sensitivity of nanocrystalline materials. Int. J. Plast. 23, 2115–2133.

Lin, Q., Chen, F., Yin, H., 2017. Experimental and theoretical investigation of the thermo-mechanical deformation of a functionally graded panel. Eng. Struct. 138, 17–26.

Lin, Q., Zhang, L., Chen, F., Yin, H., 2019. Micromechanics-based elastoplastic modeling of functionally graded materials with pairwise particle interactions. J. Eng. Mech. 145, 04019033.

Mallek, H., Jrad, H., Wali, M., Dammak, F., 2019. Nonlinear dynamic analysis of piezoelectric-bonded FG-CNTR composite structures using an improved FSDT theory. Eng. Comput., 1–19

Mareau, C., Berbenni, S., 2015. An affine formulation for the self-consistent modeling of elasto-viscoplastic heterogeneous materials based on the translated field method. Int. J. Plast. 64, 134–150.

McLaughlin, R., 1977. A study of the differential scheme for composite materials. Int. J. Eng. Sci. 15, 237–244.

Misra, A., Poorsolhjouy, P., 2015. Granular micromechanics model for damage and plasticity of cementitious materials based upon thermomechanics. Math. Mech. Solids 1081286515576821.

Misra, A., Singh, V., 2013. Micromechanical model for viscoelastic materials undergoing damage. Contin. Mech. Thermodyn. 25, 343–358.

Misra, A., Yang, Y., 2010. Micromechanical model for cohesive materials based upon pseudo-granular structure. Int. J. Solids Struct. 47, 2970–2981.

Mori, T., Tanaka, K., 1973. Average stress in matrix and average elastic energy of materials with misfitting inclusions. Acta Metall. 21, 571–574.

Moschovidis, Z.A., Mura, T., 1975. Two-ellipsoidal inhomogeneities by the equivalent inclusion method. J. Appl. Mech. 42, 847–852.

Mura, T., 2013. Micromechanics of Defects in Solids. Springer Science & Business Media.

Nemat-Nasser, S., Hori, M., 2013. Micromechanics: Overall Properties of Heterogeneous Materials. Elsevier.

Nguyen-Xuan, H., Tran, L.V., Nguyen-Thoi, T., Vu-Do, H.C., 2011. Analysis of functionally graded plates using an edge-based smoothed finite element method. Compos. Struct. 93, 3019–3039.

Ortwein, R., Skoczeń, B., Tock, J.P., 2014. Micromechanics based constitutive modeling of martensitic transformation in metastable materials subjected to torsion at cryogenic temperatures. Int. J. Plast. 59, 152–179.

Pascon, J.P., Coda, H.B., 2015. Large deformation analysis of functionally graded elastoplastic materials via solid tetrahedral finite elements. Comput. Struct. 146, 59–75.

Paulino, G.H., Yin, H.M., Sun, L.Z., 2006. Micromechanics-based interfacial debonding model for damage of functionally graded materials with particle interactions. Int. J. Damage Mech. 15, 267–288.

Pierard, O., Lorca, O., Segurado, J., Doghri, I., 2007. Micromechanics of particle-reinforced elasto-viscoplastic composites: Finite element simulations versus affine homogenization. Int. J. Plast. 23, 1041–1060.

Pompe, W., Worch, H., Epple, M., Friess, W., Gelinsky, M., Greil, P., Hempel, U., Scharnweber, D., Schulte, K., 2003. Functionally graded materials for biomedical applications. Mater. Sci. Eng. A 362, 40–60.

Reiter, T., Dvorak, G.J., 1998. Micromechanical models for graded composite materials: II. Thermomechanical loading. J. Mech. Phys. Solids 46, 1655–1673.

Reiter, T., Dvorak, G.J., Tvergaard, V., 1997. Micromechanical models for graded composite materials. J. Mech. Phys. Solids 45, 1281–1302.

Samei, J., Zhou, L., Kang, J., Wilkinson, D.S., 2018. Microstructural analysis of ductility and fracture in fine-grained and ultrafine-grained vanadium-added DP1300 steels. Int. J. Plast. 117, 58–70.

Seltzer, R., Cisilino, A.P., Frontini, P.M., Mai, Y.-W., 2011. Determination of the Drucker-Prager parameters of polymers exhibiting pressure-sensitive plastic behaviour by depth-sensing indentation. Int. J. Mech. Sci. 53, 471–478.

Simo, J.C., Hughes, T.J., 2006. Computational Inelasticity. Springer Science & Business Media.

Sun, L.Z., Ju, J.W., 2004. Elastoplastic modeling of metal matrix composites containing randomly located and oriented spheroidal particles. J. Appl. Mech. 71, 774–785.

Sun, L.Z., Ju, J.W., 2001. Effective elastoplastic behavior of metal matrix composites containing randomly located aligned spheroidal inhomogeneities. Part II: applications. Int. J. Solids Struct. 38, 203–225.

Tan, H., Huang, Y., Liu, C., Geubelle, P.H., 2005. The Mori-Tanaka method for composite materials with nonlinear interface debonding. Int. J. Plast. 21, 1890–1918.

Vena, P., Gastaldi, D., Contro, R., 2008. Determination of the effective elastic–plastic response of metal–ceramic composites. Int. J. Plast. 24, 483–508.

Yang, J., Pickard, S.M., Cady, C., Evans, A.G., Mehrabian, R., 1991. The stress/strain behavior of aluminum matrix composites with discontinuous reinforcements. Acta Metall. Mater. 39, 1863–1869.

Yin, H., Zhao, Y., 2016. Introduction to the Micromechanics of Composite Materials. CRC Press.

Yin, H.M., Paulino, G.H., Buttlar, W.G., Sun, L.Z., 2008. Effective thermal conductivity of functionally graded particulate nanocomposites with interfacial thermal resistance. J. Appl. Mech. 75, 051113.

Yin, H.M., Sun, L.Z., Paulino, G.H., 2004. Micromechanics-based elastic model for functionally graded materials with particle interactions. Acta Mater. 52, 3535–3543.

Yin, H.M., Yang, D.J., Kelly, G., Garant, J., 2013. Design and performance of a novel building integrated PV/thermal system for energy efficiency of buildings. Sol. Energy 87, 184–195.

Zuiker, J.R., 1995. Functionally graded materials: choice of micromechanics model and limitations in property variation. Compos. Eng. 5, 807–819.